Small-signal Stability of Grid-connected Converter System in Renewable Energy Systems with Fractional-order Synchronous Reference Frame Phase-locked Loop

Peng Zhang, Wenjuan Du, *Member*, *IEEE*, and Haifeng Wang, *Senior Member*, *IEEE*

Abstract—**Fractional-order control (FOC) has gained significant attention in power system applications due to their ability to enhance performance and increase stability margins. In grid-connected converter (GCC) systems, the synchronous reference frame phase-locked loop (SRF-PLL) plays a critical role in grid synchronization for renewable power generation. However, there is a notable research gap regarding the application of FOC to the SRF-PLL. This paper proposes a fractional-order SRF-PLL (FO-SRF-PLL) that incorporates FOC to accurately track the phase angle of the terminal voltage, thereby improving the efficiency of grid-connected control. The dynamic performance of the proposed FO-SRF-PLL is evaluated under varying grid conditions. A comprehensive analysis of the small-signal stability of the GCC system employing the FO-SRF-PLL is also presented, including derived small-signal stability conditions. The results demonstrate that the FO-SRF-PLL significantly enhances robustness against disturbances compared with the conventional SRF-PLL. Furthermore, the GCC system with the FO-SRF-PLL maintains stability even under weak grid conditions, showing superior stability performance over the SRF-PLL. Finally, both simulation and experimental results are provided to validate the analysis and conclusions presented in this paper.**

Index Terms—**Small-signal stability, grid-connected converter (GCC) system, fractional-order control (FOC), fractional-order synchronous reference frame phase locked loop (FO-SRF-PLL).**

I. Introduction

FRACTIONAL-ORDER elements (FOEs) and fractional-order control (FOC) have garnered significant interest in recent years within the electrical engineering community due to their enhanced flexibility and versatility in circuit design and applications [1], [2]. Similarly, FOC has emerged as a promising approach for improving system performance and efficiency [3]. In renewable energy systems, FOEs and FOC provide a powerful framework for modeling system dynamics, which can be precisely described using fractional-order (FO) differential equations.

Recent advances have explored several novel applications of FOEs. For example, a high-power FO capacitor based on power converters has been proposed [4], and FO models of filter inductors have been implemented within the control bandwidth of converters [5]. An FO modeling and analysis method for direct current (DC)-DC converters using FO inductors and capacitors was proposed in [6]. Additionally, an FO virtual capacitor aimed at active damping in multi-paralleled grid-connected current-source inverters has been introduced [7]. These innovations highlight the potential of FOEs to enhance the performance and efficiency of power electronic systems. In this paper, we use the FO model to describe the dynamics of transmission lines.

FOC, in particular, has gained significant attention as a control strategy for power and power electronic systems. Numerous studies have explored various FOC techniques, including FO proportional-integral-derivative (FOPID) control, FO sliding mode control (FOSMC), and FO terminal sliding mode control (FOTSMC). FOC has been successfully applied to enhance the robustness of multilevel converter integration into power grids [8], improve power quality in grid-connected photovoltaic (PV) systems [9], and optimize output voltage tracking in DC-DC buck converters [10]. Furthermore, FOC has been utilized in passivity-based FOSMC [11] and robust fuzzy FOTSMC for grid-connected converter (GCC) systems [12]. It has also been applied in voltage and frequency control for microgrids [13], voltage control for high-voltage direct current (HVDC) transmission systems [14], robust controller design [15], and the experimental enhancement of fuzzy FOPID controllers for variable-speed wind energy conversion systems [16]. These studies demonstrate the broad applicability and advantages of FOC in power systems and power electronic applications.

Phase-locked loops (PLLs) are a core component of modern power systems and power electronics. The synchronous reference frame PLL (SRF-PLL) has become the standard

Manuscript received: February 29, 2024; revised: June 5, 2024; accepted: September 13, 2024. Date of CrossCheck: September 13, 2024. Date of online publication: September 19, 2024.

This work was supported in part by the Natural Science Foundation of China (No. 52077144) and the Youth Innovative Research Team of Science and Technology Scheme, Sichuan Province, China (No. 22CXTD0066).

This article is distributed under the terms of the Creative Commons Attribution 4.0 International License (http://creativecommons.org/licenses/by/4.0/).

P. Zhang, W. Du (corresponding author), and H. Wang are with the School of Electrical Engineering, Sichuan University, Chengdu, China (e-mail: zzppAwj009@foxmail.com; ddwenjuan@qq.com; hfwang60@qq.com).

DOI: 10.35833/MPCE.2024.000215

for grid-connected renewable energy systems due to its efficiency, controllability, and adaptability. Several advanced PLL designs have been proposed to address power quality issues under abnormal grid conditions, such as enhanced PLL, dual second-order generalized integrator PLL, and double SRF-PLL [17]. Comparative analyses have shown that while SRF-PLL may not be as robust under certain grid conditions as some of the more advanced PLLs, it remains the predominant choice for grid connection in renewable energy systems [18], [19].

The application of fractional calculus to PLLs has also shown promising results. In [20], an FO analog PLL (FOAPLL) was introduced, demonstrating enhanced capture range and reduced lock time compared with the traditional integer-order analog PLL (IOAPLL). Subsequent studies [21], [22] analyzed the bandwidth, locking range, and transient response of FOAPLL, while [23] highlighted its superior performance in noisy environments. However, fractional calculus has yet to be applied to SRF-PLL in grid-connected control systems. Inspired by the FOAPLL model, this paper proposes an FO-SRF-PLL using FOPID control, aiming to improve the accuracy and performance of terminal voltage phase tracking.

Despite the growing use of FOEs and FOC in power systems, their application to SRF-PLL for grid-connected renewable energy systems remains unexplored. This paper introduces the FO-SRF-PLL for grid-connected control systems and investigates the small-signal stability of GCC systems employing the FO-SRF-PLL. The contributions of this paper are described as follows.

1) The FO-SRF-PLL, utilizing FOPID control for terminal voltage phase tracking in GCC systems, is proposed. The FO-SRF-PLL outperforms its integer-order counterpart in terms of faster response, higher tracking accuracy, and quicker settling time under varying grid conditions.

2) A linearized model of GCC systems with FO-SRF-PLL is derived, along with stability criteria specific to these systems.

3) Small-signal stability conditions for GCC systems employing the FO-SRF-PLL are derived. Simulation and experimental results demonstrate that the FO-SRF-PLL significantly improves small-signal stability, especially in weak grid connections, compared with conventional SRF-PLL.

The remainder of this paper is organized as follows. Section II evaluates the performance of the proposed FO-SRF-PLL. Section III presents the linear model derivation of the GCC system with FO-SRF-PLL. The stability analysis is discussed in Section IV. Section V presents simulation and experimental results under varying grid conditions to validate the proposed FO-SRF-PLL. Finally, Section VI concludes this paper.

II. Performance Evaluation of FO-SRF-PLL

A. FO-SRF-PLL

The FO-SRF-PLL is developed by applying the FOPID controller proposed in [24] to the conventional SRF-PLL. Figure 1 shows the structural block diagram of the FO-SRF-PLL, where the FO proportional-integral (FOPI) controller and FO integrator (FOI) are used in the FO-SRF-PLL. In Fig. 1, V_{ga}, V_{gb}, and V_{gc} are the input three-phase voltages; V_{gd} and V_{gq} are the d-axis and q-axis voltages obtained by coordinate transformation, respectively; K_p and K_i are the proportional gain and integral gain of the FOPI controller, respectively; ω_0 is the nominal frequency; and α is the order of the FOPI controller and the FOI. The output of the FOI is the phase angle θ_p estimated by the FO-SRF-PLL. The conventional SRF-PLL can be seen as a special case of the FO-SRF-PLL with $\alpha = 1$.

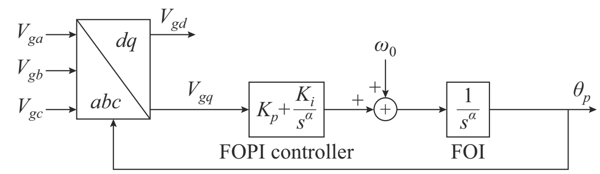

Fig. 1. Structural block diagram of FO-SRF-PLL.

Figure 2 shows the linear model of the proposed FO-SRF-PLL, where V_{g0} is the magnitude of the input voltage; x_p is the output of the FOI in the FOPI controller; and θ is the phase of the input voltage. The closed-loop transfer function of the estimated phase θ_p to the actual phase θ is:

$$\frac{\theta_p(s)}{\theta(s)} = \frac{V_{g0}\left(K_p s^\alpha + K_i\right)}{s^{2\alpha} + V_{g0} K_p s^\alpha + V_{g0} K_i} \tag{1}$$

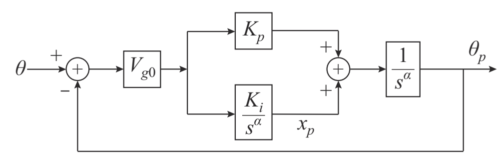

Fig. 2. Linear model of FO-SRF-PLL.

In this paper, the subscript "0" is used to denote the steady-state value of the variable or variable vector.

B. Implementation of FO-SRF-PLL

The implementation of an FOPID controller typically requires a rational approximation. The Oustaloup filter algorithm (OFA) [25] is commonly used for the continuous-time approximation in the numerical implementation of FO systems. Within the considered frequency band $\left(\omega_b, \omega_h\right)$, s^α can be approximated by:

$$G(s) = K \prod_{k=1}^{N} \frac{s + \omega'_k}{s + \omega_k} \tag{2}$$

where N is the order of the filter; $K = \omega_h^\alpha$; $\omega'_k = \omega_b \omega_u^{(2k-1-\alpha)/N}$, $\omega_k = \omega_u^{2\alpha/N} \omega'_k$, and $\omega_u = \sqrt{\omega_h/\omega_b}$.

In the paper, the above FOA is used for realization of FOPID controllers, and the approximated FOPID transfer function is:

$$H(s) = K_p + K_i \left(K \prod_{k=1}^{N} \frac{s + \omega'_k}{s + \omega_k} \right)_{-\alpha} \tag{3}$$

With respect to the digital implementation, the Tustin discretization method is used for FO-SRF-PLL [26].

C. Performance Evaluation of FO-SRF-PLL

The performance of the proposed FO-SRF-PLL is evaluated under varying grid conditions. To simulate realistic grid operations, the 9-bus test system described in [18] is used, as shown in Fig. 3 (active and reactive power flows are in MW and Mvar, respectively). The system is modeled in MATLAB/Simulink, with bus 6 selected as the point of common coupling (PCC) for integrating the GCC system. The testing scheme and implementation details are provided in Table I.

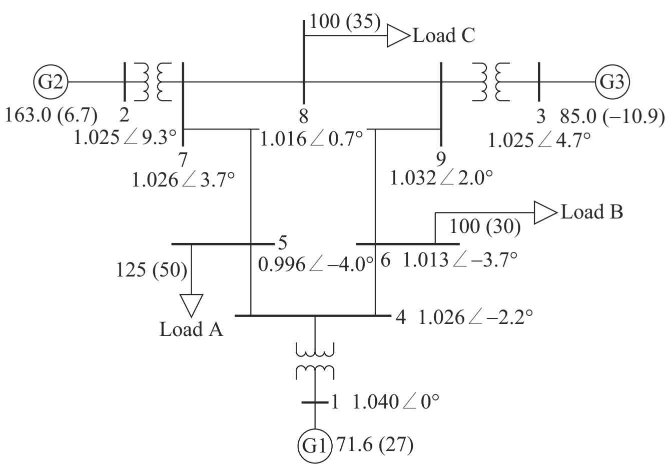

Fig. 3. Power flow diagram of test system.

TABLE I
TESTING SCHEME AND IMPLEMENTATION DETAILS

Testing scheme	Condition	Implementation detail
Conducted on test system	Under-voltage	An inductive load of +j150 Mvar connected to bus 6 at 60 ms
	Over-voltage	A capacitive load of −j80 Mvar connected to bus 6 at 60 ms
	Load rise	Load at buses 6 and 9 increased by 100 MW+j100 Mvar at 60 ms
Utilizing a three-phase programmable voltage source	Phase jump	Phase jump of $\pi/6$ radians at 50 ms
	Frequency step	Frequency step of 2 Hz at 50 ms

Table II provides the performance evaluation metrics of PLL, including locking time, overshoot/undershoot, and settling time. Locking time refers to the duration required from receiving the input signal to achieving signal lock. The PCC voltage V_{abc}, q-axis voltage V_q, and estimated phase θ under different test conditions are depicted in Figs. 4-8.

Table II and Figs. 4-8 show that the locking time of the SRF-PLL is significantly longer than that of the FO-SRF-PLL. Across various test scenarios, the locking time of the SRF-PLL is at least ten times longer than that of the FO-SRF-PLL. Furthermore, the GCC system using the FO-SRF-PLL exhibits a lower transient peak overshoot/undershoot and a quicker recovery response compared with the SRF-PLL.

TABLE II
PERFORMANCE EVALUATION METRICS OF PLL

Condition	PLL	Locking time (ms)	Overshoot/undershoot (%)	Settling time (ms)
Under-voltage	SRF-PLL	46.5	5.9	23.5
	FO-SRF-PLL	4.4	0.4	2.9
Over-voltage	SRF-PLL	46.5	100.0	30.0
	FO-SRF-PLL	4.4	88.8	5.4
Load rise	SRF-PLL	46.5	9.5	7.3
	FO-SRF-PLL	4.4	1.5	2.0
Phase jump	SRF-PLL	25.0	49.2	16.0
	FO-SRF-PLL	1.2	47.1	1.0
Frequency step	SRF-PLL	25.0	61.0	16.0
	FO-SRF-PLL	1.2	59.0	1.0

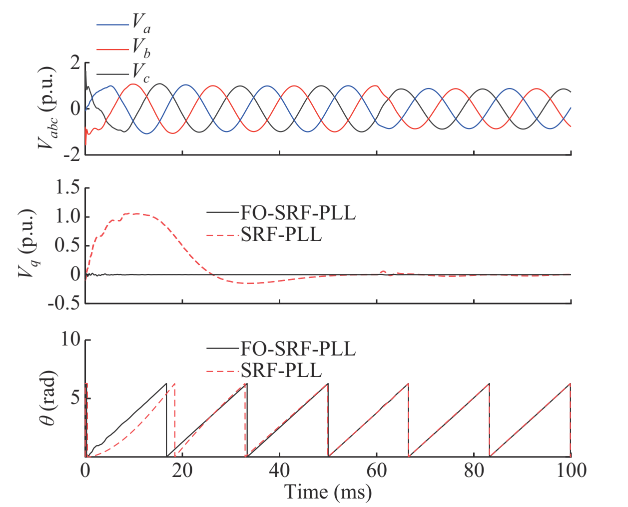

Fig. 4. Transient response to under-voltage conditions.

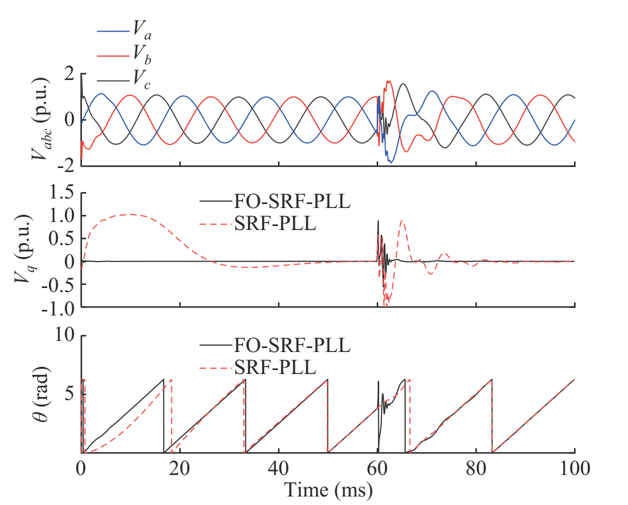

Fig. 5. Transient response to over-voltage conditions.

In general, the FO-SRF-PLL demonstrates a significantly faster locking time, reduced undershoot/overshoot and shorter settling time compared with the SRF-PLL. This enhanced performance allows for quicker and more accurate tracking of the desired phase in the GCC system.

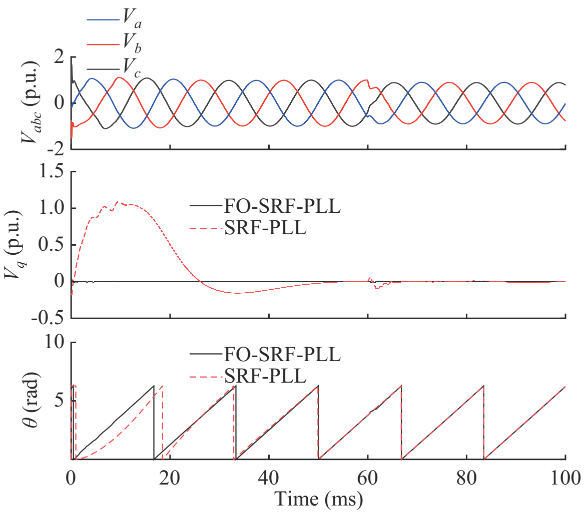

Fig. 6. Transient response to load rise conditions.

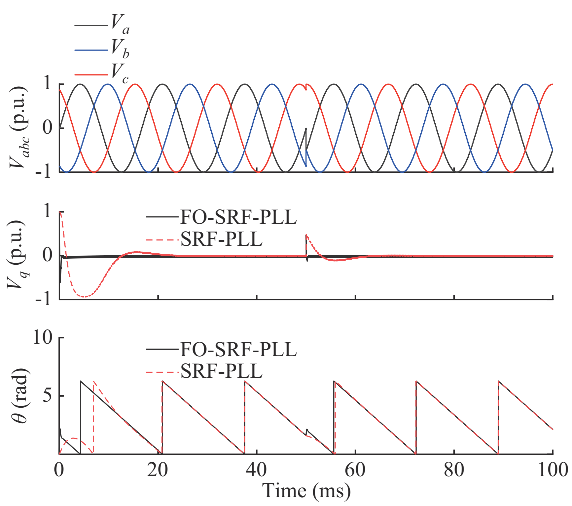

Fig. 7. Transient response to a phase jump.

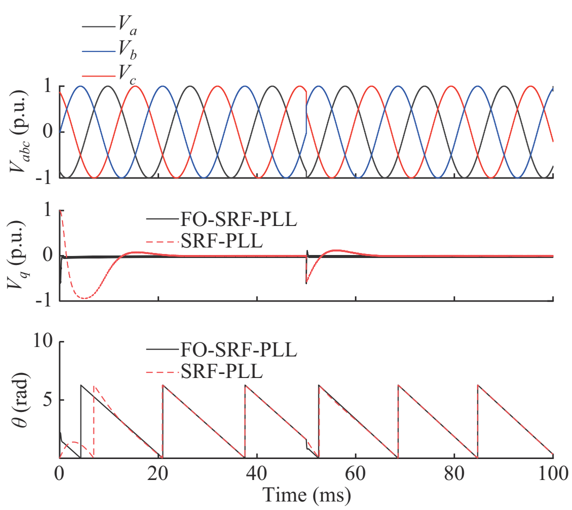

Fig. 8. Transient response to a frequency step.

III. Linear Model Derivation of GCC System with FO-SRF-PLL

Figure 9 shows the configuration of the GCC system in renewable energy systems, where V is the converter output voltage; V_g is the PCC voltage; I is the converter output current; V_b is the grid voltage; I_d and I_q are the d- and q-axis components of the GCC output current, respectively; I_{dref} and I_{qref} are the reference values of the d- and q-axis currents of the current control loop, respectively; θ_p is the phase angle estimated by the PLL; L_f is the filter inductance; and L_g is the transmission line inductance.

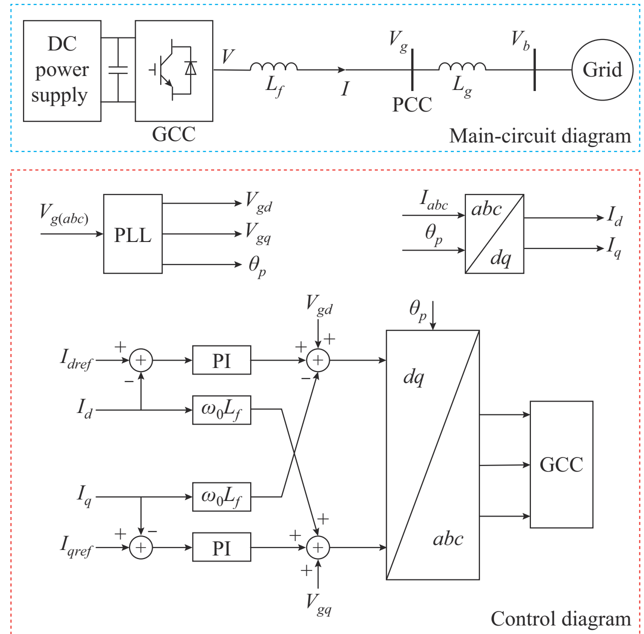

Fig. 9. Configuration of GCC system in renewable energy systems.

The GCC system shown in Fig. 9 is commonly used in PV or wind power systems, employing closed-loop control of the output current. The closed-loop control of the output current in the GCC system is realized in d-q coordinate. Moreover, in practical scenarios, the bandwidth of the inner loop of the current control is typically much greater than that of the PLL. Therefore, when assessing the stability of small disturbances associated with the PLL dynamics, it is reasonable to consider the output current of the GCC as equal to the current reference value provided by the inner loop of the current control. Consequently, the GCC can be represented as a constant current source, i. e., $I_{d0}+\mathrm{j}I_{q0}$. Hence, we can obtain:

$$\Delta I_d+\mathrm{j}\Delta I_q=0 \tag{4}$$

In the paper, prefix Δ refers to a small increment of the variable or variable vector.

Figure 10 shows the equivalent circuit and phasor diagram of the GCC system in the d-q coordinate, where $V_{g0}\angle 0$ is the PCC voltage; X_g is the transmission line reactance; and $V_{b0}\angle -\delta$ is the voltage of the alternating current (AC) grid. From Fig. 10, the voltage amplitude V_{g0} can be obtained as:

$$V_{g0}=\sqrt{V_{b0}^2-I_{d0}^2X_g^2}-I_{q0}X_g \tag{5}$$

The d-q coordinate is aligned by continuously tracking the phase angle of PCC voltage using the PLL. From Fig. 2, the FO differential equations of FO-SRF-PLL can be obtained as:

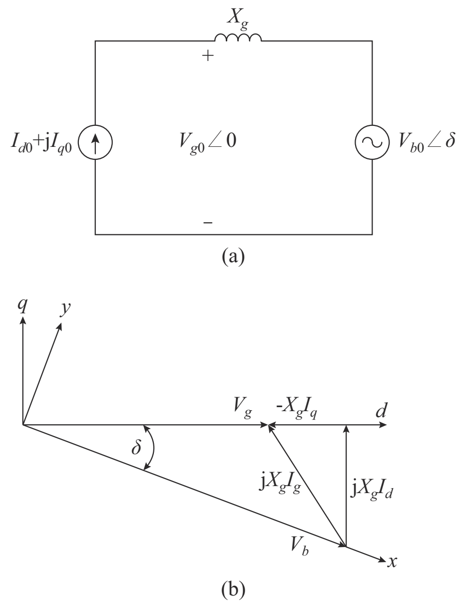

Fig. 10. Equivalent circuit and phasor diagram of GCC system in *d-q* coordinate. (a) Equivalent circuit. (b) Phasor diagram.

$$\begin{cases}\dfrac{\mathrm{d}^\alpha x_p}{\mathrm{d}t^\alpha}=K_iV_{g0}\left(\theta-\theta_p\right)\\[2mm] \dfrac{\mathrm{d}^\alpha \theta_p}{\mathrm{d}t^\alpha}=K_pV_{g0}\left(\theta-\theta_p\right)+x_p\end{cases}\tag{6}$$

Figure 11 shows the relationship between the *d-q* coordinate and the common *x-y* coordinate. The PLL utilizes the tracked phase of the PCC voltage to determine the orientation of the *d*-axis in the common *x-y* coordinate.

$$\Delta\theta=\begin{bmatrix}-\dfrac{V_{gy0}}{V_{g0}^2} & \dfrac{V_{gx0}}{V_{g0}^2}\end{bmatrix}\begin{bmatrix}\Delta V_{gx}\\ \Delta V_{gy}\end{bmatrix}=\begin{bmatrix}-\dfrac{V_{gy0}}{V_{g0}^2} & \dfrac{V_{gx0}}{V_{g0}^2}\end{bmatrix}\Delta\boldsymbol{V}_{gxy}\tag{7}$$

where subscript x and y are used to indicate the x and y component of the variable or variable vector in the common *x-y* coordinate.

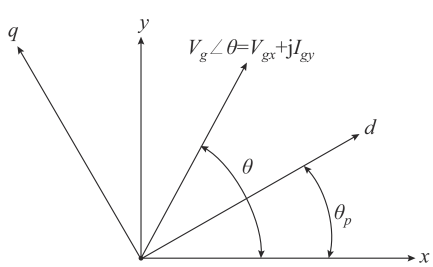

Fig. 11. Relationship between *x-y* and *d-q* coordinates.

Then, we have:

$$\begin{aligned}\begin{bmatrix}I_x\\ I_y\end{bmatrix}&=\begin{bmatrix}\cos\theta_p & -\sin\theta_p\\ \sin\theta_p & \cos\theta_p\end{bmatrix}\begin{bmatrix}I_d\\ I_q\end{bmatrix}\\ \begin{bmatrix}I_d\\ I_q\end{bmatrix}&=\begin{bmatrix}\cos\theta_p & \sin\theta_p\\ -\sin\theta_p & \cos\theta_p\end{bmatrix}\begin{bmatrix}I_x\\ I_y\end{bmatrix}\end{aligned}\tag{8}$$

Thus, from (4) and (8), we can obtain:

$$\Delta\boldsymbol{I}_{xy}=\begin{bmatrix}\Delta I_x\\ \Delta I_y\end{bmatrix}=\begin{bmatrix}-I_{y0}\\ I_{x0}\end{bmatrix}\Delta\theta_p\tag{9}$$

The linearization of (6) is:

$$\begin{cases}\dfrac{\mathrm{d}^\alpha \Delta x_p}{\mathrm{d}t^\alpha}=K_iV_{g0}\left(\Delta\theta-\Delta\theta_p\right)\\[2mm] \dfrac{\mathrm{d}^\alpha \Delta\theta_p}{\mathrm{d}t^\alpha}=K_pV_{g0}\left(\Delta\theta-\Delta\theta_p\right)+\Delta x_p\end{cases}\tag{10}$$

From (7), (9) and (10), we can obtain:

$$\begin{cases}\dfrac{\mathrm{d}^\alpha \Delta\boldsymbol{X}}{\mathrm{d}t^\alpha}=\boldsymbol{A}\Delta\boldsymbol{X}+\boldsymbol{B}\Delta\boldsymbol{V}_{gxy}\\ \Delta\boldsymbol{I}_{xy}=\boldsymbol{C}\Delta\boldsymbol{X}\\ \Delta\boldsymbol{X}=\begin{bmatrix}\Delta x_p\\ \Delta\theta_p\end{bmatrix}\\ \boldsymbol{A}=\begin{bmatrix}0 & -K_iV_{g0}\\ 1 & -K_pV_{g0}\end{bmatrix}\\ \boldsymbol{B}=\begin{bmatrix}-\dfrac{K_iV_{gy0}}{V_{g0}} & \dfrac{K_iV_{gx0}}{V_{g0}}\\ -\dfrac{K_pV_{gy0}}{V_{g0}} & \dfrac{K_pV_{gx0}}{V_{g0}}\end{bmatrix}\\ \boldsymbol{C}=\begin{bmatrix}0 & -I_{y0}\\ 0 & I_{x0}\end{bmatrix}\end{cases}\tag{11}$$

The FO model of transmission lines is built as:

$$\begin{cases}\dfrac{X_g}{\omega_0}\dfrac{\mathrm{d}^\alpha I_x}{\mathrm{d}t^\alpha}=V_{gx}-V_{bx}+X_gI_y\\[2mm] \dfrac{X_g}{\omega_0}\dfrac{\mathrm{d}^\alpha I_y}{\mathrm{d}t^\alpha}=V_{gy}-V_{by}-X_gI_x\end{cases}\tag{12}$$

Ignoring the dynamics of the grid, the linearization of (12) is:

$$\begin{cases}\dfrac{\mathrm{d}^\alpha \Delta I_x}{\mathrm{d}t^\alpha}=\dfrac{\omega_0}{X_L}\Delta V_{gx}+\Delta\omega_0 I_y\\[2mm] \dfrac{\mathrm{d}^\alpha \Delta I_y}{\mathrm{d}t^\alpha}=\dfrac{\omega_0}{X_L}\Delta V_{gy}-\Delta\omega_0 I_x\end{cases}\tag{13}$$

Or, equivalently, we can obtain:

$$\Delta\boldsymbol{V}_{gxy}=X_g\begin{bmatrix}\dfrac{s^\alpha}{\omega_0} & -1\\ 1 & \dfrac{s^\alpha}{\omega_0}\end{bmatrix}\Delta\boldsymbol{I}_{xy}=\left(\dfrac{X_gs^\alpha}{\omega_0}\boldsymbol{U}_1+X_g\boldsymbol{U}_2\right)\Delta\boldsymbol{I}_{xy}\tag{14}$$

where $\boldsymbol{U}_1=\begin{bmatrix}1 & 0\\ 0 & 1\end{bmatrix}$; and $\boldsymbol{U}_2=\begin{bmatrix}0 & -1\\ 1 & 0\end{bmatrix}$.

Let P_0 and Q_0 be the steady-state active and reactive power outputs of the GCC system, then we have:

$$\begin{cases}P_0=I_{x0}V_{gx0}+I_{y0}V_{gy0}\\ Q_0=I_{x0}V_{gy0}-I_{y0}V_{gx0}\end{cases}\tag{15}$$

From (9), (11), (14), and (15), we can obtain:

$$\frac{\mathrm{d}^\alpha\Delta\boldsymbol{X}}{\mathrm{d}^\alpha}=\left(\boldsymbol{U}_1-\frac{X_g}{\omega_0}\boldsymbol{BC}\right)^{-1}\left(\boldsymbol{A}+X_g\boldsymbol{BU}_2\boldsymbol{C}\right)\Delta\boldsymbol{X}=\boldsymbol{A}_c\Delta\boldsymbol{X}\tag{16}$$

$$\begin{cases} \boldsymbol{A}_c = \dfrac{1}{d}\begin{bmatrix} a & b \\ 1 & c \end{bmatrix} \\ a = \dfrac{X_g K_i P_0}{\omega_0 V_{g0}} \\ b = \left(1 - \dfrac{X_g K_p P_0}{\omega_0 V_{g0}}\right)\left(\dfrac{X_g K_i Q_0}{V_{g0}} - K_i V_{g0}\right) + \\ \quad \dfrac{X_g K_i P_0}{\omega_0 V_{g0}}\left(\dfrac{X_g K_p Q_0}{V_{g0}} - K_p V_{g0}\right) \\ c = \dfrac{X_g K_p Q_0}{V_{g0}} - K_p V_{g0} \\ d = 1 - \dfrac{X_g K_p P_0}{\omega_0 V_{g0}} \end{cases} \tag{17}$$

Next, the objective is to analyze the stability of system (16).

IV. Small-signal Stability Analysis of GCC System with FO-SRF-PLL

In fractional calculus, the FO linear time-invariant (FO-LTI) system is represented as follows:

$$\begin{cases} D^q \boldsymbol{x} = \boldsymbol{A}\boldsymbol{x} + \boldsymbol{B}\boldsymbol{u} \\ \boldsymbol{y} = \boldsymbol{C}\boldsymbol{x} \end{cases} \tag{18}$$

where $D^q = \mathrm{d}^q/\mathrm{d}t^q$ is the fractional differential operator; and q is the order of derivation.

It has been demonstrated that the system in (18) is stable when (19) is satisfied [27], where $\mathrm{eig}(\boldsymbol{A})$ denotes the eigenvalues of matrix $\boldsymbol{A}$, and the argument of $\mathrm{eig}(\boldsymbol{A})$ is denoted by $\arg(\mathrm{eig}(\boldsymbol{A}))$. Figure 12 shows the stable and unstable regions of system in (18) with $0 < q \le 1$.

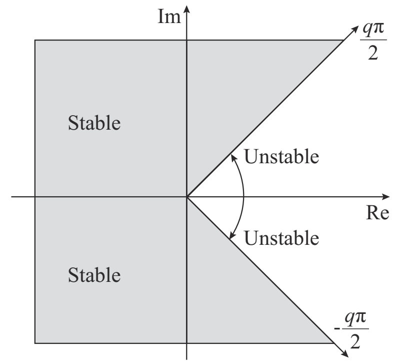

Fig. 12. Stable and unstable regions of system in (18) with $0 < q \le 1$.

$$\left|\arg\left(\mathrm{eig}(\boldsymbol{A})\right)\right| \frac{q\pi}{2} \tag{19}$$

The following theorem establishes a crucial condition for confining the eigenvalues of a matrix within specific sectors. It serves as the foundation for establishing a direct association between the stability of LTI systems and FO-LTI systems.

Theorem 1 [28]: if and only if the LTI system in (20) is asymptotically stable, the system in (18) with $0 < q \le 1$ is unstable.

$$\dot{\boldsymbol{x}} = -\begin{bmatrix} \boldsymbol{A}\sin\left(\dfrac{q\pi}{2}\right) & -\boldsymbol{A}\cos\left(\dfrac{q\pi}{2}\right) \\ \boldsymbol{A}\cos\left(\dfrac{q\pi}{2}\right) & \boldsymbol{A}\sin\left(\dfrac{q\pi}{2}\right) \end{bmatrix}\boldsymbol{x} \tag{20}$$

In this paper, the objective is to determine the parameters that render the FO-LTI system in (21) stable.

$$D^\alpha \Delta\boldsymbol{X} = \boldsymbol{A}_c \Delta\boldsymbol{X} \tag{21}$$

where $0 < \alpha \le 1$ is given.

From theorem 1, the equivalent LTI system in terms of stability for the FO-LTI system (21) can be expressed as:

$$\begin{cases} \dfrac{\mathrm{d}\Delta\boldsymbol{X}}{\mathrm{d}t} = \boldsymbol{A}_e \Delta\boldsymbol{X} \\ \boldsymbol{A}_e = \begin{bmatrix} -\dfrac{a\sin(\alpha\pi/2)}{d} & -\dfrac{b\sin(\alpha\pi/2)}{d} & \dfrac{a\cos(\alpha\pi/2)}{d} & \dfrac{b\cos(\alpha\pi/2)}{d} \\ -\dfrac{\sin(\alpha\pi/2)}{d} & -\dfrac{c\sin(\alpha\pi/2)}{d} & \dfrac{\cos(\alpha\pi/2)}{d} & \dfrac{c\cos(\alpha\pi/2)}{d} \\ -\dfrac{a\cos(\alpha\pi/2)}{d} & -\dfrac{b\cos(\alpha\pi/2)}{d} & -\dfrac{a\sin(\alpha\pi/2)}{d} & -\dfrac{b\sin(\alpha\pi/2)}{d} \\ -\dfrac{\cos(\alpha\pi/2)}{d} & -\dfrac{c\cos(\alpha\pi/2)}{d} & -\dfrac{\sin(\alpha\pi/2)}{d} & -\dfrac{c\sin(\alpha\pi/2)}{d} \end{bmatrix} \end{cases} \tag{22}$$

Therefore, the instability of the GCC system with the FO-SRF-PLL is equivalent to the stability of the system in (22). The system in (22) has the following characteristic polynomial:

$$P(s) = s^4 + a_3 s^3 + a_2 s^2 + a_1 s + a_0 = 0 \tag{23}$$

$$\begin{cases} a_0 = (ac-b)^2/d^4 \\ a_1 = 2\sin(\alpha\pi/2)(a+c)(ac-b)/d^3 \\ a_2 = \left(2b - 4b\sin^2(\alpha\pi/2) + a^2 + c^2 + 4ac\sin^2(\alpha\pi/2)\right)/d^2 \\ a_3 = 2\sin(\alpha\pi/2)(a+c)/d \end{cases} \tag{24}$$

Supplementary Material A demonstrates that the instability conditions of the system described by (21) are given by (25) and further verifies the correctness of (25).

$$\begin{cases} d > 0 \\ a + c > 0 \\ ac - b > 0 \\ (a+c)^2 - 4(ac-b)\cos^2(\alpha\pi/2) > 0 \quad \alpha \in (0,1] \end{cases} \tag{25}$$

Supplementary Material B demonstrates that the GCC system described by (16) is unstable if and only if conditions in (26) are satisfied. The small-signal instability conditions in (26) can be utilized to evaluate the stability of the GCC system.

$$\begin{cases} X_g < \dfrac{V_{g0}\omega_0}{K_p P_0} \\ X_g > \dfrac{K_p V_{g0}^2 \omega_0}{K_i P_0 + K_p Q_0 \omega_0} \\ \left(K_p V_{g0} - \dfrac{K_p Q_0 X_g}{V_{g0}} - \dfrac{K_i P_0 X_g}{V_{g0}\omega_0}\right)^2 - \\ \quad \dfrac{4K_i \cos^2(\alpha\pi/2)\left(V_{g0}^2 - Q_0 X_g\right)\left(V_{g0}\omega_0 - K_p P_0 X_g\right)}{V_{g0}^2 \omega_0} > 0 \end{cases} \tag{26}$$

For $\alpha = 1$, it can be proven that the GCC system employing SRF-PLL is stable if and only if conditions in (27) are satisfied.

$$\begin{cases} X_g < \dfrac{V_{g0}\omega_0}{K_p P_0} \\ X_g < \dfrac{K_p V_{g0}^2 \omega_0}{K_i P_0 + K_p Q_0 \omega_0} \end{cases} \tag{27}$$

It can be observed from (26) that the stability of the system is influenced by the operating conditions of the GCC system as well as the values of K_p and K_i in the FO-SRF-PLL.

V. Simulation and Experimental Results

A. Simulation Results

The system shown in Fig. 9 has been built in MATLAB/Simulink to verify the accuracy of the theoretical analysis in this paper. Assume that the system operates with a power factor of 1 and the nominal voltage is 1 p.u., which implies $Q_0 = 0$, i.e., $I_{q0} = 0$. For ease of calculation, let $V_{b0} = \sqrt{10}/3 \approx 1.054$, and $\alpha = 0.5$. Thus, we can obtain:

$$V_{g0} = \sqrt{10 - 9I_{d0}^2 X_g^2}\Big/3 \tag{28}$$

To facilitate a comparative analysis of the stability of GCC the system with the SRF-PLL and FO-SRF-PLL, the following stability conditions are provided for the system when SRF-PLL is employed, as well as the instability conditions when FO-SRF-PLL with $\alpha = 0.5$ is utilized.

From (27) and (28), the stability conditions for the GCC system with the SRF-PLL are obtained.

$$\begin{cases} X_g < \dfrac{\omega_0}{K_p I_{d0}} \\ X_g^2 < \dfrac{10K_p^2\omega_0^2}{9K_p^2\omega_0^2 I_{d0}^2 + K_i^2} \end{cases} \tag{29}$$

From (26) and (28), when the FO-SRF-PLL with $\alpha = 0.5$ is utilized, the GCC system is unstable if and only if:

$$\begin{cases} X_g < \dfrac{\omega_0}{K_p I_{d0}} \\ X_g^2 > \dfrac{10K_p^2\omega_0^2}{9K_p^2\omega_0^2 I_{d0}^2 + K_i^2} \\ X_g^2 > 10 - \left\{\dfrac{-K_i}{K_i^2 - K_p^2\omega_0^2}\left[3\omega_0^2 - \sqrt{9\omega_0^4 + 10\left(K_i^2 - K_p^2\omega_0^2\right)}\right]\right\}^2 \end{cases} \tag{30}$$

Three tests have been conducted to validate the theoretical analysis. The results regarding the impact of the PLL control parameters K_p and K_i on the small-signal stability of the system are presented below. Moreover, the impacts of the transmission line reactance X_g and the steady-state active power P_0 are detailed in Supplementary Material C.

To evaluate the impact of K_p, we have conducted the following test. The reactance of the transmission line is fixed to be $X_g = 1$, and $I_{d0} = 1/3$. Thus, $V_{g0} = 1$, and $P_0 = V_{g0} I_{d0} = 1/3$. K_i is fixed to be ω_0^2 ($\omega_0 = 2\pi f = 120\pi$). From (29), the stability condition for the GCC system with SRF-PLL is:

$$125.66 \approx 40\pi = \frac{1}{3}\omega_0 < K_p < 3\omega_0 = 360\pi \approx 1130.97 \tag{31}$$

Supplementary Material D shows that there does not exist a value of K_p that would lead to instability in the GCC system with the FO-SRF-PLL. The nonlinear simulation results are depicted in Figs. 13-16. For all these tests, P corresponds to the active power output from the GCC. At 0.1 s of simulation, the active power output from the GCC in the example system increases by 10% for 100 ms.

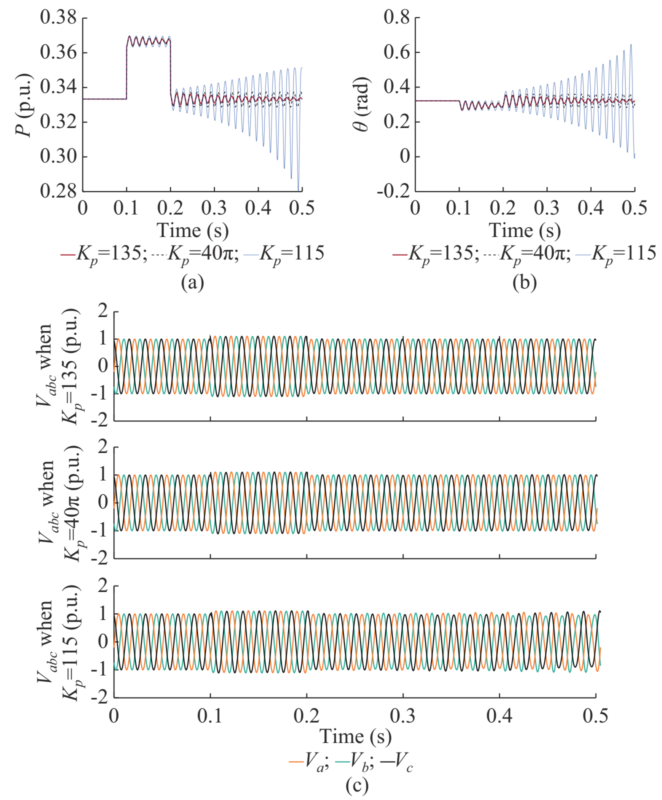

Fig. 13. Results of nonlinear simulation with variation of K_p in SRF-PLL. (a) P. (b) θ. (c) V_{abc}.

It can be observed from Figs. 13-16 that when the value of K_p exceeds the upper and lower limits obtained in (31), the GCC system with SRF-PLL becomes unstable, whereas the system with FO-SRF-PLL remains unaffected by the changes of K_p.

To evaluate the impact of K_i, the following test is conducted. The system parameters are set to the same as before, and the value of K_p is fixed to be $\omega_0/3$. From (29), the stability condition for the GCC system with the SRF-PLL is:

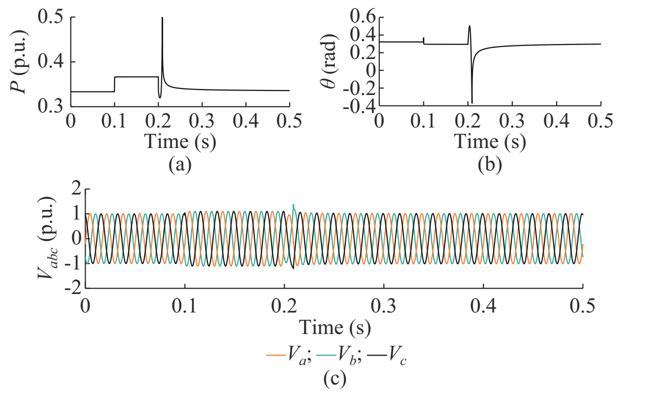

Fig. 14. Results of nonlinear simulation with $K_p = 0.1$ in FO-SRF-PLL. (a) P. (b) θ. (c) V_{abc}.

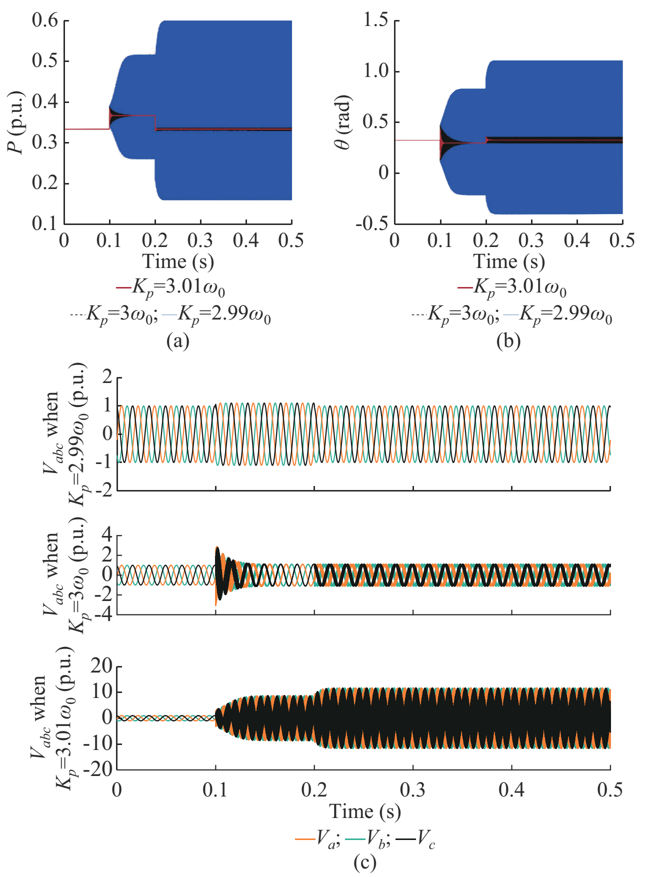

Fig. 15. Results of nonlinear simulation with variation of K_p in SRF-PLL. (a) P. (b) θ. (c) V_{abc}.

$$K_i \omega_0^2 \approx 1.42 \times 10^5 \tag{32}$$

Similarly, there is no value of K_i that would result in instability of the GCC system with the FO-SRF-PLL. The nonlinear simulation results are depicted in Figs. 17 and 18. Clearly, while the GCC system with the SRF-PLL loses stability due to the value of K_i exceeding the range obtained in (32), the system with the FO-SRF-PLL remains stable.

This test effectively validates the accuracy of the instability conditions by varying the control parameters of the PLL. Furthermore, it can be observed that when the system stability is constrained by the values of K_p and K_i in the GCC system with SRF-PLL, the stability of the system remains unaffected by the values of K_p and K_i in the GCC system with FO-SRF-PLL. This finding highlights the robustness of the proposed FO-SRF-PLL in maintaining system stability under varying control parameters.

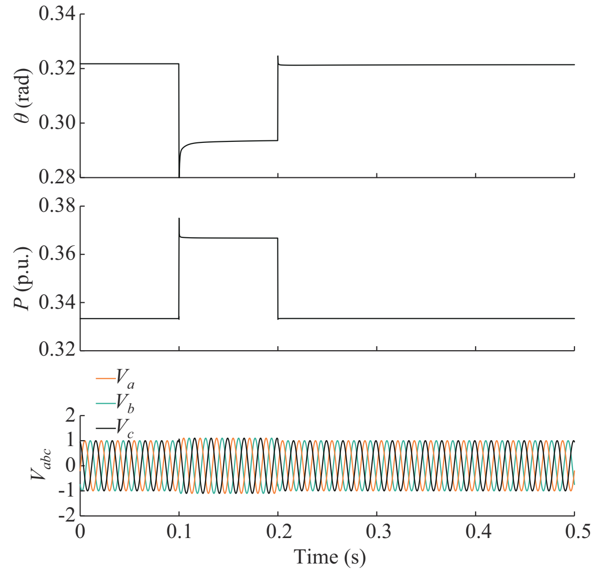

Fig. 16. Results of nonlinear simulation with $K_p = 100\omega_0$ in FO-SRF-PLL.

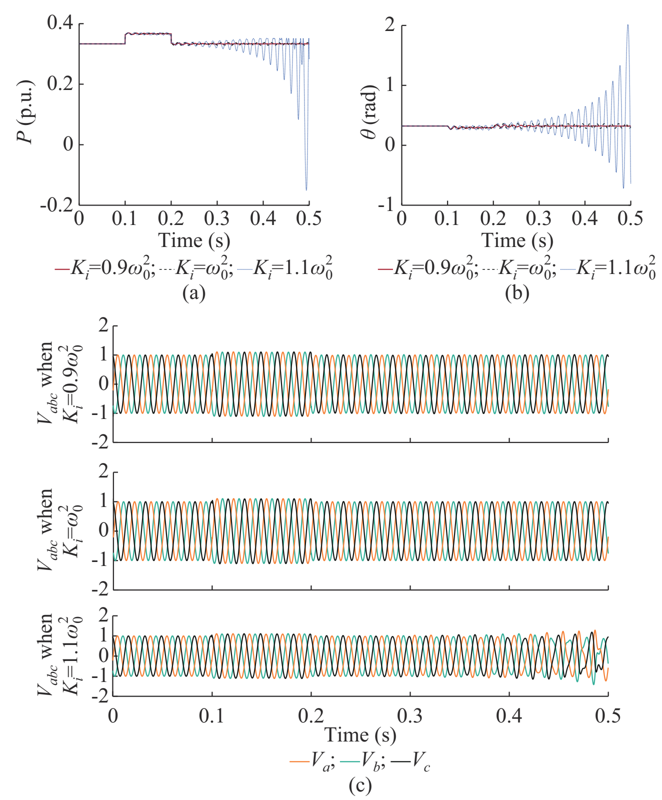

Fig. 17. Results of nonlinear simulation with variation of K_i in SRF-PLL. (a) P. (b) θ. (c) V_{abc}.

B. Experimental Results

This subsection aims to evaluate the performance of the proposed FO-SRF-PLL and to verify the correctness of the theoretical analysis through experimental results. A hardware-in-the-loop (HIL) experimental platform is established, as shown in Fig. 19, and the main parameters are detailed in Table III.

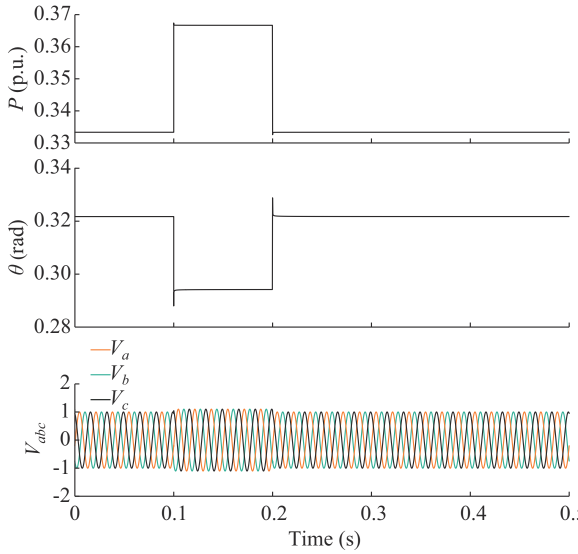

Fig. 18. Results of nonlinear simulation with $K_i = 50\omega_0^2$ in FO-SRF-PLL.

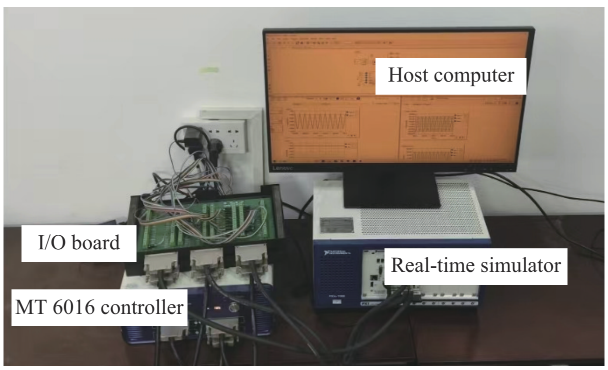

Fig. 19. HIL experimental platform.

TABLE III
MAIN EXPERIMENTAL PARAMETERS

Parameter	Value	Parameter	Value
DC-side voltage V_{dc}	200 V	OFA parameters (ω_b, ω_h)	$(10^{-2}, 10^5)$
Filter inductor L_f	5.25 mH	PLL proportional gain K_p	0.01-50
Grid impedance L_g	3-15 mH	PLL integral gain K_i	300-5000
Grid phase voltage V_b	78 V	Current loop proportional coefficient K_{cp}	0.15
Switching frequency f_w	10 kHz	Current loop integral coefficient K_{ci}	60
Sampling frequency f_s	10 kHz	Current reference of d-axis I_{d0}	10-30 A
Order of Oustaloup filter N	5	Current reference of d-axis I_{q0}	0

1) Performance Evaluation of FO-SRF-PLL

The performance of the FO-SRF-PLL is evaluated under a phase jump condition. The transient response to a phase jump of $\pi/3$ radians at 100 ms is shown in Fig. 20. The PCC voltage response, q-axis voltage response, and phase angle tracking output results using the SRF-PLL and FO-SRF-PLL under the phase jump condition are shown in Fig. 20(a) and 20(b), respectively. Table IV presents the performance evaluation metrics, including locking time, overshoot, and settling time. Experimental results show that the FO-SRF-PLL exhibits faster locking time, reduced overshoot, and shorter settling time.

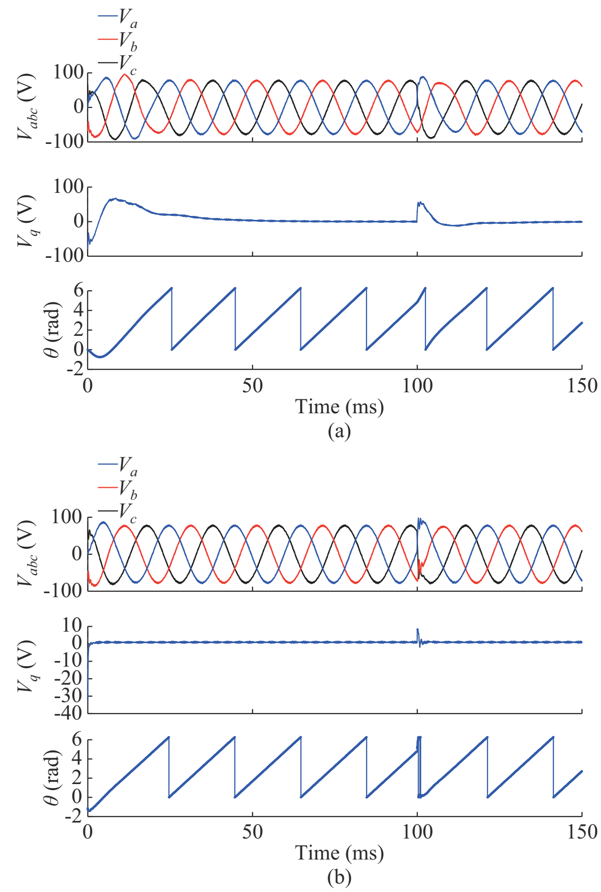

Fig. 20. PCC voltage, q-axis voltage, and phase angle tracking output results under phase angle jump condition. (a) SRF-PLL. (b) FO-SRF-PLL.

TABLE IV
PERFORMANCE EVALUATION METRICS UNDER PHASE ANGLE JUMP CONDITION

Type	Locking time (ms)	Overshoot (%)	Settling time (ms)
SRF-PLL	55.2	5800	38
FO-SRF-PLL	5.6	870	6

2) Verification of Small-signal Stability Analysis

The experimental waveforms of PCC voltage and active power of the GCC system when K_p changes are given in the test ($I_{d0} = 10$ A, $L_g = 7.5$ mH, $K_i = 300$). When K_p increases and decreases, the experimental results of the GCC system with the SRF-PLL and the FO-SRF-PLL are shown in Figs. 21 and 22, respectively. The active power output increases by 10% within 150 to 160 ms. From the experimental results, it is clear that when K_p increases from 10 to 15 or decreases from 10 to 0.1, the GCC system with the SRF-PLL loses stability. In contrast, the GCC system with the FO-SRF-PLL remains stable even when K_p increases from 10 to 50 or decreases from 10 to 0.01. While the GCC system using the SRF-PLL loses stability due to the change of K_p, the GCC system with the FO-SRF-PLL can remain stable.

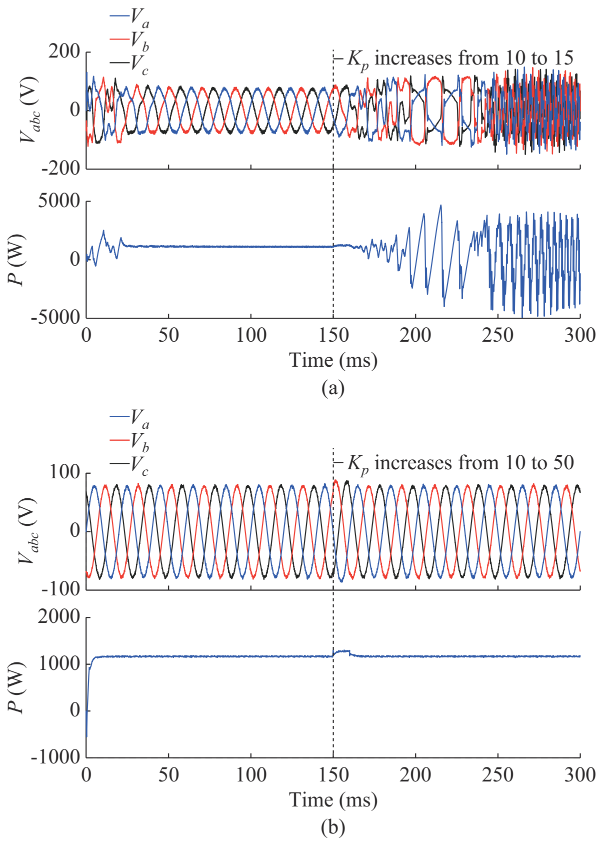

Fig. 21. Experimental results of GCC system when K_p increases. (a) SRF-PLL. (b) FO-SRF-PLL.

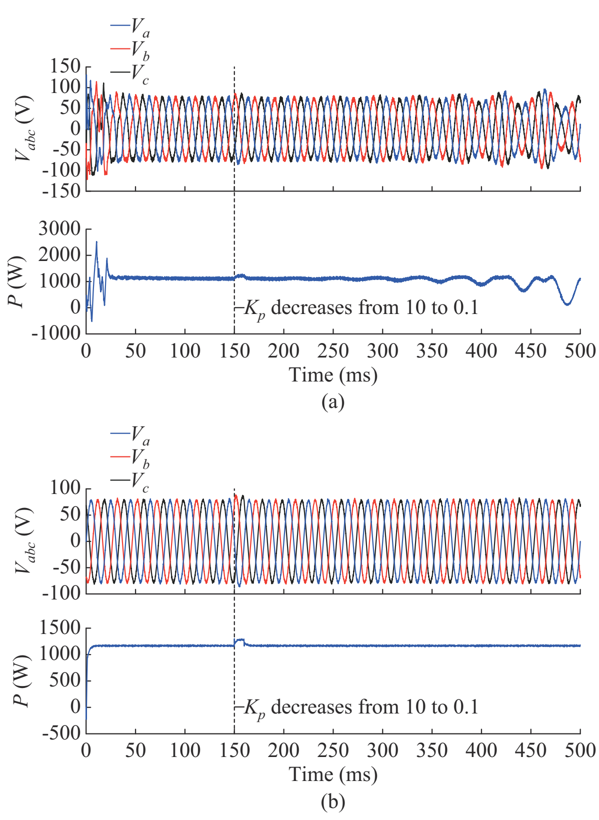

Fig. 22. Experimental results of GCC system when K_p decreases. (a) SRF-PLL. (b) FO-SRF-PLL.

The experimental waveforms of PCC voltage and output active power of the GCC system during variations in K_i are presented in this test, with $I_{d0}=10$ A, $L_g=7.5$ mH, $K_p=10$. The results of the GCC system with the SRF-PLL and the FO-SRF-PLL are shown in Fig. 23. It is evident from the results that as K_i increases from 300 to 3000, the GCC system with the SRF-PLL loses stability, while the GCC system with the FO-SRF-PLL remains stable even when K_i increases from 300 to 5000. Compared with the SRF-PLL, the GCC system with FO-SRF-PLL has a lower risk of instability when K_i changes.

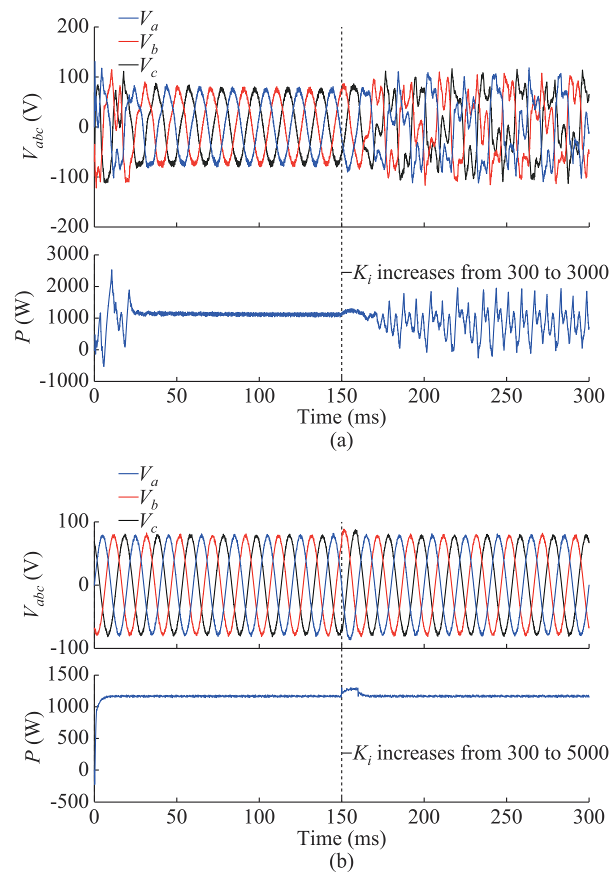

Fig. 23. Experimental results of GCC system when K_i increases. (a) SRF-PLL. (b) FO-SRF-PLL.

The experimental results of PCC voltage and output active power of the GCC system when I_{d0} changes are given in this test, with $L_g=7.5$ mH, $K_p=10$, and $K_i=300$. The results of the GCC system with the SRF-PLL and the FO-SRF-PLL are shown in Fig. 24. It can be observed from the results that when I_{d0} changes, i. e., P_0 changes, the GCC system with SRF-PLL loses stability, whereas the GCC system with FO-SRF-PLL remains stable. Compared with the SRF-PLL, the stability of the GCC system with FO-SRF-PLL is less affected by changes in P_0.

The experimental results under varying L_g with $I_{d0}=10$ A, $K_p=10$, and $K_i=300$ are shown in Fig. 25. It can be observed that as L_g increases, the instability risk of the GCC system with SRF-PLL increases, while the stability of the GCC system using FO-SRF-PLL is not affected.

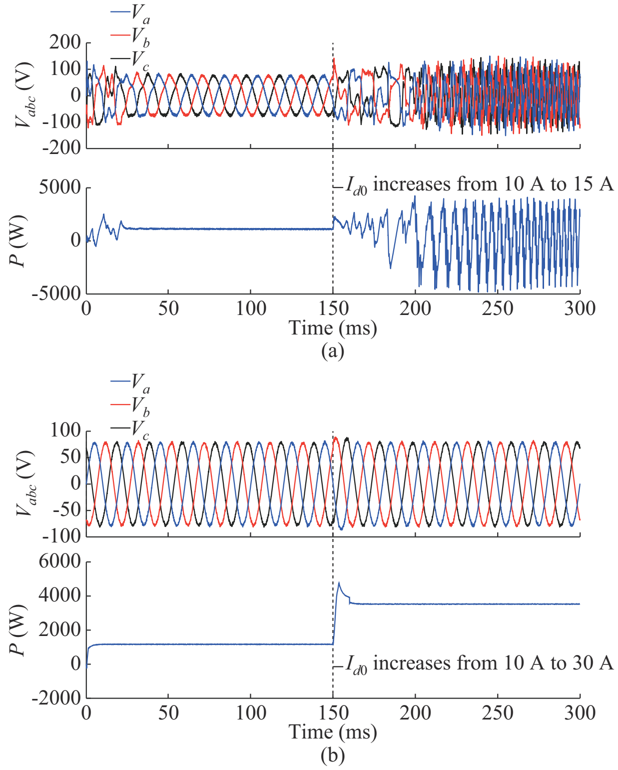

Fig. 24. Experimental results of GCC system when changing given current. (a) SRF-PLL. (b) FO-SRF-PLL.

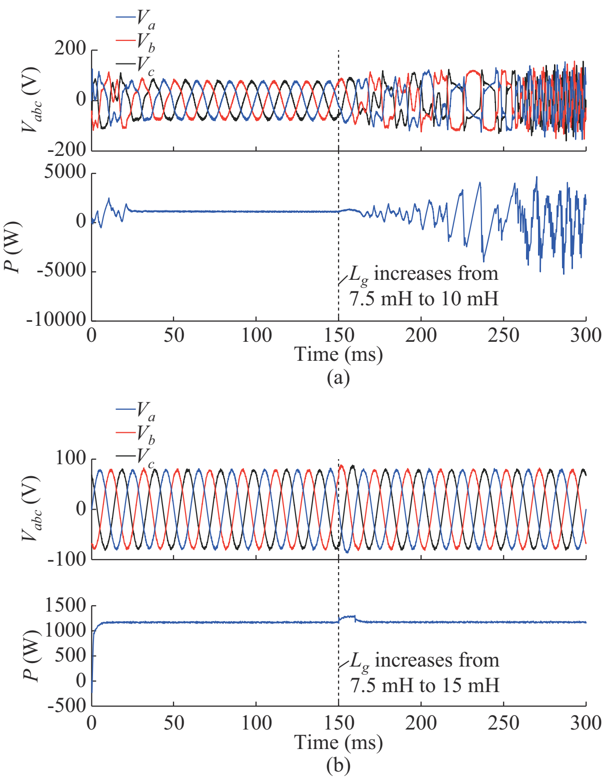

Fig. 25. Experimental results of GCC system when L_g is changed. (a) SRF-PLL. (b) FO-SRF-PLL.

In summary, the performance of the FO-SRF-PLL proposed in this paper is significantly superior to that of the SRF-PLL. The locking time and settling time are considerably shorter, and the maximum error value during step changes is reduced. Furthermore, the GCC system using SRF-PLL tends to lose stability under small disturbances when the control and operating parameters change, whereas the GCC system with FO-SRF-PLL remains stable. The experimental results verify the effectiveness of the proposed FO-SRF-PLL.

VI. Conclusion

This paper introduces an FO-SRF-PLL for accurate phase angle tracking of the terminal voltage in GCC systems. The stability conditions of GCC system with FO-SRF-PLL are derived and analyzed. Through simulation and experimental results, several useful conclusions are drawn as follows.

1) The utilization of the FO-SRF-PLL demonstrates reduced undershoot, faster response, and shorter settling time. These improved performances enable quicker and more precise tracking of the desired phase in GCC system.

2) GCC system with the SRF-PLL may become unstable due to changes in the PLL control parameters. However, the stability of GCC system with FO-SRF-PLL is less likely to be affected by variations in control parameters.

3) As the steady-state active power and the transmission line reactance increase, GCC system with FO-SRF-PLL exhibits greater stability compared with that with the SRF-PLL. Notably, even with extremely weak grid connections, GCC system with the FO-SRF-PLL remains stable.

Further research and investigation are required to explore the potential applications of FOC and FOEs in renewable energy systems and their impact on system stability. This paper serves as an initial exploration, and future work should focus on expanding the understanding of these techniques and their implementation.

References

[1] I. Petras, *Fractional-order Nonlinear Systems*. Berlin: Springer Verlag, 2011, pp. 47-52.

[2] M. S. Sarafraz and M. S. Tavazoei, "Passive realization of fractional-order impedances by a fractional element and RLC components: conditions and procedure," *IEEE Transactions on Circuits and Systems I: Regular Papers*, vol. 64, no. 3, pp. 585-595, Mar. 2017

[3] D. Pullaguram, S. Mishra, N. Senroy *et al*., "Design and tuning of robust fractional order controller for autonomous microgrid VSC system," *IEEE Transactions on Industry Applications*, vol. 54, no. 1, pp. 91-101, Feb. 2018.

[4] Y. Jiang and B. Zhang, "High-power fractional-order capacitor with $1<\alpha<2$ based on power converter," *IEEE Transactions on Industrial Electronics*, vol. 65, no. 4, pp. 3157-3164, Apr. 2018.

[5] S. F. Chou, X. Wang, and F. Blaabjerg, "A fractional-order model of filter inductors within converter control bandwidth," in *Proceedings of 2018 IEEE Electronic Power Grid (eGrid)*, Charleston, USA, Nov. 2018, pp. 1-6.

[6] X. Chen, Y. Chen, B. Zhang *et al*., "A modeling and analysis method for fractional-order DC-DC converters," *IEEE Transactions on Power Electronics*, vol. 32, no. 9, pp. 7034-7044, Sept. 2017.

[7] M. A. Azghandi, S. M. Barakati, and A. Yazdani, "Passivity-based design of a fractional-order virtual capacitor for active damping of multiparalleled grid-connected current-source inverters," *IEEE Transactions on Power Electronics*, vol. 37, no. 7, pp. 7809-7818, Jul. 2022.

[8] A. Zafari, M. Mehrasa, S. Bacha *et al*., "A robust fractional-order control technique for stable performance of multilevel converter-based grid-tied DG units," *IEEE Transactions on Industrial Electronics*, vol. 69, no. 10, pp. 10192-10201, Oct. 2022.

[9] M. Badoni, A. Singh, S. Pandey *et al*., "Fractional-order Notch filter for grid-connected solar PV system with power quality improvement,"

IEEE Transactions on Industrial Electronics, vol. 69, no. 1, pp. 429-439, Jan. 2022.

[10] B. Babes, S. Mekhilef, A. Boutaghane *et al*., "Fuzzy approximation-based fractional-order nonsingular terminal sliding mode controller for DC-DC buck converters," *IEEE Transactions on Industrial Electronics*, vol. 37, no. 3, pp. 2749-2760, Mar. 2022.

[11] B. Long, W. Mao, P. Lu *et al*., "Passivity fractional-order sliding-mode control of grid-connected converter with LCL filter," *IEEE Transactions on Industrial Electronics*, vol. 38, no. 6, pp. 6969-6982, Jun. 2023.

[12] B. Long, P. Lu, K. Chong *et al*., "Robust fuzzy-fractional-order nonsingular terminal sliding-mode control of LCL-type grid-connected converters," *IEEE Transactions on Industrial Electronics*, vol. 69, no. 6, pp. 5854-5866, Jun. 2022.

[13] M. K. Behera and L. C. Saikia, "An improved voltage and frequency islanded microgrid using BPF based droop control and optimal third harmonic injection PWM scheme," *IEEE Transactions on Industry Applications*, vol. 58, no. 2, pp. 2483-2496, Apr. 2022.

[14] R. Shah, R. Preece, and M. Barnes, "The impact of voltage regulation of VSC-HVDC on power system stability," *IEEE Transactions on Energy Conversion*, vol. 33, no. 4, pp. 1614-1627, Dec. 2018.

[15] S. Ghasemi, A. Tabesh, and J. Askari-Marnani, "Application of fractional calculus theory to robust controller design for wind turbine generators," *IEEE Transactions on Energy Conversion*, vol. 29, no. 3, pp. 780-787, Sept. 2014.

[16] A. Beddar, H. Bouzekri, B. Babes *et al*., "Experimental enhancement of fuzzy fractional order PI+I controller of grid connected variable speed wind energy conversion system," *Energy Conversion and Management*, vol. 123, no. 1, pp. 569-580, Sept. 2016.

[17] M. E. Meral and D. Çelík, "A comprehensive survey on control strategies of distributed generation power systems under normal and abnormal conditions," *Annual Reviews in Control*, vol. 47, pp. 112-132, Dec. 2018.

[18] V. Khatana and R. Bhimasingu, "Review on three-phase PLLs for grid integration of renewable energy sources," in *Proceedings of 2017 14th IEEE India Council International Conference (INDICON)*, Roorkee, India, Dec. 2017, pp. 1-6.

[19] S. Golestan, J. M. Guerrero, and J. C. Vasquez, "Three-phase PLLs: a review of recent advances," *IEEE Transactions on Power Electronics*, vol. 32, no. 3, pp.1894-1907, May 2016.

[20] R. El-Khazali and W. Ahmad, "Fractional-order phase-locked loop," in *Proceedings of 2007 9th International Symposium on Signal Processing and Its Applications*, Sharjah, United Arab Emirates, Feb. 2007, pp. 1-4.

[21] M. C. Tripathy, D. Mondal, K. Biswas *et al*., "Design and performance study of phase-locked loop using fractional-order loop filter," *International Journal of Circuit Theory and Applications*, vol. 43, no. 6, pp. 776-792, Jun. 2015.

[22] B. T. Krishna, "Fractional calculus-based analysis of phase locked loop," in *Proceedings of 2012 International Conference on Signal Processing and Communications (SPCOM)*, Bangalore, India, Aug. 2012, pp. 1-5.

[23] R. El-Khazali, W. Ahmad, and Z. A. Memon, "Noise performance of fractional-order phase-locked loop," in *Proceedings of 2007 IEEE International Conference on Signal Processing and Communications*, Dubai, United Arab Emirates, Nov. 2007, pp. 572-575.

[24] I. Podlubny, "Fractional-order systems and $PI_{\lambda}D_{\mu}$-controllers," *IEEE Transactions on Automatic Control*, vol. 44, no. 1, pp. 208-214, Jan. 1999.

[25] A. Oustaloup, F. Levron, B. Mathieu *et al*., "Frequency-band complex noninteger differentiator: characterization and synthesis," *IEEE Transactions on Circuits and Systems I: Fundamental Theory and Applications*, vol. 47, no.1, pp. 25-39, Jan. 2000.

[26] C. A. Monje, Y. Chen, B. M. Vinagre *et al*., *Fractional-Order Systems and Controls*. London: Springer, 2010, pp. 193-198.

[27] D. Matignon, "Stability result on fractional differential equations with applications to control processing," *Computational Engineering in Systems Applications*, vol. 2, no. 1, pp. 963-968, Jul. 1996.

[28] M. S. Tavazoei and M. Haeri, "A note on the stability of fractional order systems," *Mathematics and Computers in Simulation*, vol. 79, no. 5, pp. 1566-1576, Jan. 2009.

Peng Zhang received the B.Eng. and M.Eng. degrees in electrical engineering from Central South University, Changsha, China, in 2017 and 2020, respectively. He is currently pursuing the Ph.D. degree in Sichuan University, Chengdu, China. His research interests include power system stability analysis and application of fractional-order control in power system.

Wenjuan Du received the Ph.D. degree from the University of Bath, Bath, UK, in 2009. She is currently a Full Professor with the College of Electrical Engineering, Sichuan University, Chengdu, China. Her research interests include power system stability analysis and control, including energy storage system, flexible alternating current transmission system (FACTS), electric vehicle, and renewable power generation.

Haifeng Wang received the Ph.D. degree from Southeast University, Nanjing, China, in 1988. He is currently a Full Professor with the College of Electrical Engineering, Sichuan University, Chengdu, China. He had worked in the U.K. for years serving as the Chair of Electrical Engineering and a Full Professor at Queen's University Belfast, Belfast, U.K.. His main research interests include power system stability analysis and control.